RSC Advances

PAPER

View Article Online
View Journal | View Issue

Cite this: *RSC Adv.*, 2021, **11**, 35141

Enhanced open-circuit voltages and efficiencies: the role of oxidation state of molybdenum oxide buffer layer in polymer solar cells†

Pengfei Ma,[a] Jiaying Xu,*[a] Chen Wang,[c] Changhao Wang,[a] Fanxu Meng,*[b] Yupeng Xie[a] and Shanpeng Wen[c]

Received 16th September 2021
Accepted 22nd October 2021

DOI: 10.1039/d1ra06929b

rsc.li/rsc-advances

Molybdenum oxide (MoO_x) is widely used as a buffer layer in optoelectronic devices to improve the charge extraction efficiency. The oxidation state of MoO_x plays an important role in determining its electrical properties. However, there are few studies on the oxidation state to further guide the optimization of the MoO_x buffer layer. In this work, inverted-structured polymer solar cells (PSCs) with a MoO_x buffer layer were fabricated. Post-air annealing was used to control the cation valence state in MoO_x. X-ray photoelectron spectroscopy (XPS), ultraviolet photoelectron spectroscopy (UPS), atomic force microscopy (AFM) and transient photocurrent (TPC) were employed to study the valence state, energy level, morphology of the MoO_x layers and the photovoltaic property and charge transfer efficiency of the devices. It was found that the oxidation state was effectively improved by the post-annealing process. As a result, the work function of MoO_x was raised and the hole mobility was improved. The open-circuit voltages and the efficiencies of PTB7-Th:$PC_{71}BM$ based PSCs were enhanced from 0.77 V and 8.66% to 0.81 V and 10.01%, respectively. The results show that high oxidation state MoO_x provides optimized energy level alignment, reduced defects and better charge transfer efficiency, which is more in line with the requirement of buffer layer materials for optoelectronic applications.

Introduction

Organic photovoltaics is considered as a promising technology for harvesting energy from solar radiation owing to the potential advantages of stability, low cost, light weight, flexibility and large-scale fabrication.[1–5] Recently, polymer solar cells (PSCs) have been significantly developed with power conversion efficiencies (PCEs) over 18%.[6–8] These encouraging results not only rely on the design and synthesis of new materials and the microstructure optimization of the active layer,[9–13] but this is also inseparable from the exploration of device fabrication technologies and electrode interface engineering.[14–16] The application of inverted structures has made significant contribution to improve the performance and stability of PSCs, owing to the advantages of vertical phase separation of the active layer and reduction of reaction with water and oxygen.[17–19]

The development of electrode buffer materials and interface modification engineering also plays an important role in the improvement of PCE.[20–23] High work function (WF) transition-metal oxides such as molybdenum oxide (MoO_x), vanadium oxide, and tungsten oxide are generally used as hole transport layer (HTL) to improve charge extraction efficiency in inverted structure devices.[24–27] Among them, MoO_x have demonstrated promising potential of non-toxic nature, easy evaporation, high carrier mobility and suitable energy levels.[28–31] However, the evaporated MoO_x film generally contains oxygen vacancies. These oxygen vacancies provide additional electrons like n-type doping and change the MoO_x to lower oxidation state.[32–34] As a result, the Fermi level of MoO_x shifts toward the conduction band and the WF was decreased, which may decrease the built-in electric field at polymer/MoO_x interface and thus lower the open-circuit voltage (V_{OC}) of PSCs. Moreover, the oxygen vacancies may also act as traps for interfacial carrier recombination, resulting in energy losses. Considering the decreased WF of MoO_x can also directly affects the level alignment between MoO_x and organic active layer heterojunction, the efficiency of charge transfer at polymer/MoO_x interface, which is relied on suitable level alignment, will further influenced by the oxidation state.

In this work, we attempt to reduce the performance degradation of PSCs caused by low oxidation state in MoO_x layer by air annealing. During the inverted PSCs fabrication process, MoO_x films were deposited by thermal evaporation followed by thermal annealing in air atmosphere. It was found that all the

[a]College of Science, Jilin Institute of Chemical Technology, Jilin 132022, P. R. China. E-mail: xujiaying@jlict.edu.cn

[b]Center of Analysis and Measurement, Jilin Institute of Chemical Technology, Jilin 132022, P. R. China. E-mail: mfxoped2019@126.com

[c]State Key Laboratory on Integrated Optoelectronics and College of Electronic Science & Engineering, Jilin University, Changchun 130012, P. R. China

† Electronic supplementary information (ESI) available. See DOI: 10.1039/d1ra06929b

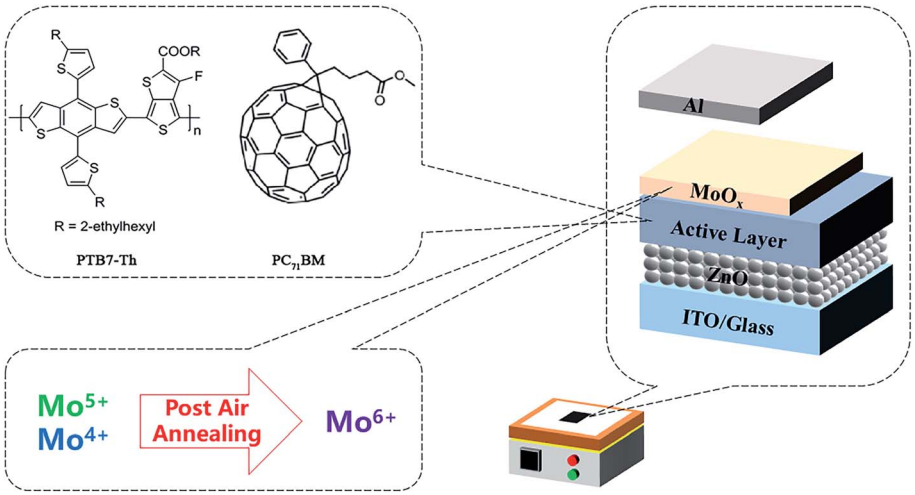

Fig. 1 Illustration of the chemical structures of active layer materials, the device structure and the post-air annealing treatment.

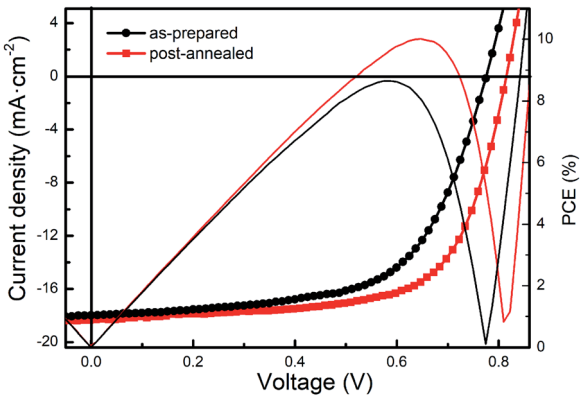

Fig. 2 *J–V* curves and PCEs of the as-prepared and post air-annealed PSCs based on PTB7-Th.

parameters of PSCs were improved especially for the V_{OC}s. We further investigated the oxidation state, morphology, energy level structure of the MoO_x layers and charge transfer in the devices. This study will provide optimized technological parameters for the fabrication of MoO_x layer and theoretical basis for applications in optoelectronic devices.

Results and discussion

Fig. 1 illustrate the post-air annealing treatment, the device structure and the chemical structures of active layer materials. PSCs with inverted structure of ITO/ZnO/PTB7-Th:$PC_{71}BM$/MoO_x/Al were fabricated. Firstly, to investigate the effect of air annealing on photovoltaic performance, the devices were annealed in air after MoO_x layer deposited. Fig. 2 shows the current density–voltage (*J–V*) curves and PCEs of as-prepared and post-annealed devices. It can be found that the V_{OC}s were markedly improved form 0.77 V to 0.81 V and the FFs were also improved from 62.12% to 67.35% by post-annealing treatment. The photovoltaic parameters are listed in Table 1. As a result, a champion PCE of 10.01% was achieved by post-annealed devices, compared with 8.66% of as-prepared devices. These results reveal that post-annealing treatment can effectively improve the performance of PSCs.

Then we cast the post-annealing treatment in glovebox as control to verify the role of air in the above process. Fig. 3 shows the *J–V* curves. Unlike air annealing, post-annealing in glovebox did not make difference to the V_{OC}s. Only the J_{SC}s and FFs were slightly larger than the as-prepared devices, which improve the PCEs less than 0.2%. Hence it can be concluded that the air is the key factor in the post-annealing.

To ensure the improvement was resulted from post-annealing of MoO_x layer, only active layer annealed devices, which were annealed in air before MoO_x layer deposited, were fabricated as control. As Fig. 3 shows, the V_{OC} and J_{SC} of active layer annealed devices were very closed to the as-prepared devices, but the FF was reduced signally. Hence the PCE was also reduced to 7.79%. Therefore, it was MoO_x layer which

Table 1 Photovoltaic parameters of the solar cells based on PTB7-Th:$PC_{71}BM$ with different annealed conditions

	V_{OC} (V)	J_{SC} (mA cm^{-2})	FF (%)	PCE (%)	
				Max.	Aver.
As-prepared devices	0.77 ± 0.01	17.68 ± 0.33	61.33 ± 0.89	8.66	8.38
Post-air annealed devices	0.81 ± 0.01	18.20 ± 0.24	66.78 ± 0.57	10.01	9.84
Annealed in glovebox	0.77 ± 0.01	18.11 ± 0.29	62.17 ± 0.41	8.84	8.68
Only active layer annealed	0.77 ± 0.01	17.70 ± 0.12	56.11 ± 0.51	7.79	7.68

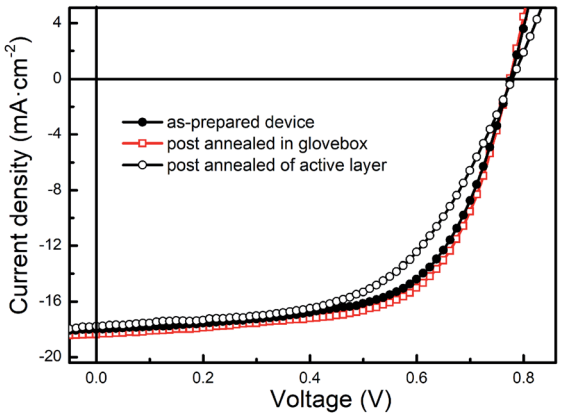

Fig. 3 *J–V* curves of the PTB7-Th-based PSCs which were as-prepared, post-annealed in glovebox and only active layer annealed.

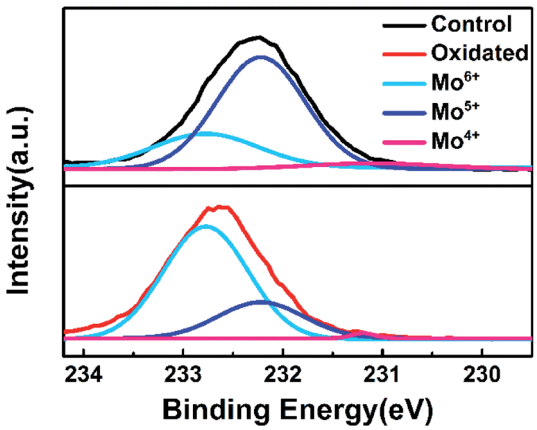

Fig. 4 The XPS spectra of Mo 3d state for as-deposited and post-annealed MoO_x films.

improved by air annealing treatment, and thus contributed to PSCs performance.

The above findings encouraged us to find out how the air annealing affect the MoO_x layer. X-ray photoelectron spectroscopy (XPS) was used to investigate the chemical compositions and cation oxidation state of MoO_x films. The experimental and fitted XPS spectra of Mo 3d state for as-deposited and post-annealed MoO_x films were shown in Fig. 4. The Mo 3d peak of post-annealed MoO_x shifted to higher binding energy compared to the as-deposited one, which indicate the proportion of Mo^{6+} in MoO_x films was increased after air annealing. According to reported literature, oxygen vacancies can be created during the evaporation in vacuum, so reduced oxidation states (Mo^{4+} and Mo^{5+}) are created by electrons trapped in such oxygen vacancies.[32] By air-annealing treatment, the vacancies were filled with oxygen atoms, the electrons were transferred from Mo atoms, and thus the oxidation states of MoO_x was enhanced. The reduced oxygen vacancies will restrain the carrier recombination in interface and promote the hole extraction of MoO_x.

The larger proportion of Mo^{6+} may raise the WF. Then we performed ultraviolet photoelectron spectroscopy (UPS) measurements to verify the energy levels of the MoO_x. As Fig. 5(a) shows, the WF of MoO_x was raised from 5.12 eV to 5.45 eV after air-annealing. This can be explained by the fact that the oxygen vacancies in MoO_x make neighbored Mo^{6+} gain electrons which can move freely within the film, like n-type doping cases. Combined with the XPS results, it can be inferred that air-annealing transfers Mo^{5+} or Mo^{4+} back to Mo^{6+} and restrains excess electron generation, and thus raise the WF.[33] Fig. 5(b) shows the energy level diagram of PTB7-Th and MoO_x. When the WF of MoO_x raised, the PTB7-Th donor's energy bands were more bended ($\Delta E_2 > \Delta E_1$). Stronger built-in electric field was formed at polymer/MoO_x interface, which may contribute to the increased V_{OC}s. Meanwhile, more efficient charge extraction can be expected to reduce the accumulated space charge and restrain the recombination at interface.

To further understand how post-annealing affects charge extraction in devices, transient photocurrent (TPC) measurements were carried out from PSCs as-prepared and post-annealed in air. As Fig. 6(a) shows, the transients of post-annealed devices decay more quickly. The characteristic time was decreased from 4.3 μs to 2.7 μs. The hole mobilities were also measured by SCLC method. We fabricated hole-only devices with configuration of ITO/PEDOT:PSS/PTB7-Th:PC_{71}-BM/MoO_x/Ag and measured the *J–V* curves which is shown in Fig. 6(b) on a semilogarithmic scale. The post-annealed devices exhibit higher charge transport efficiency. After air annealing, the

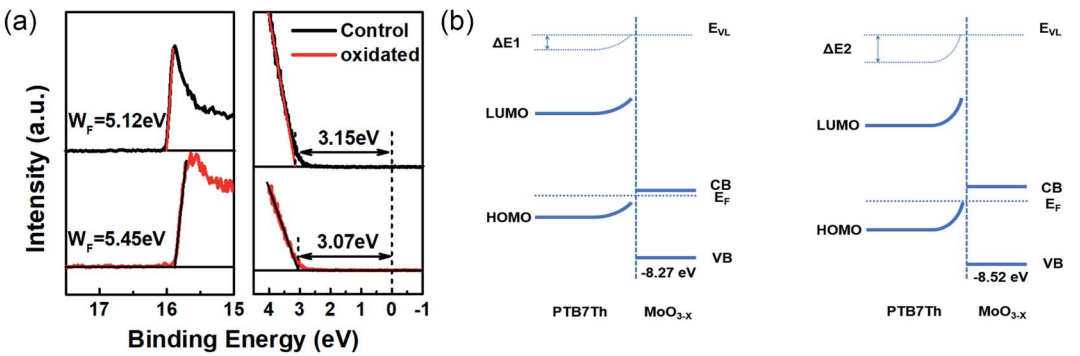

Fig. 5 (a) UPS spectra of MoO_x films measured before and after air annealing; (b) energy band diagram at PTB7-Th/MoO_x interfaces for MoO_x as-deposited (left) and post-annealed (right).

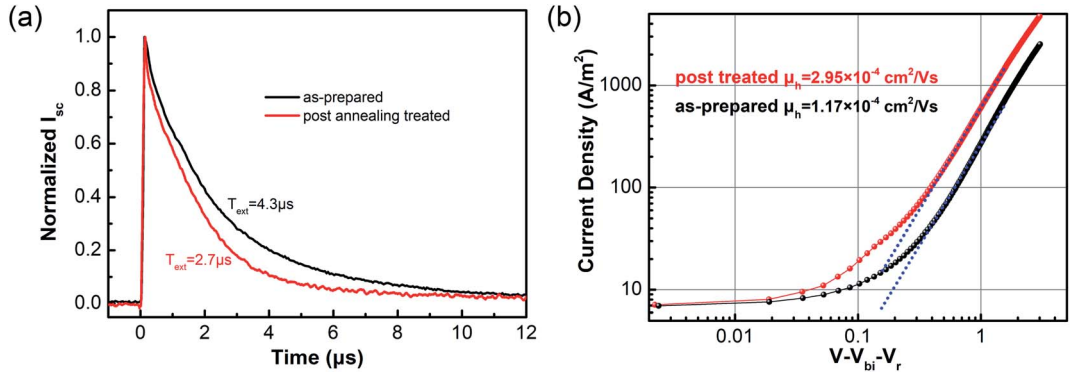

Fig. 6 (a) The normalized TPC curves of PTB7-Th-based PSCs with as-prepared and post-annealing treated MoO_x; (b) dark J–V curves of hole-only devices with as-prepared and post-annealing treated MoO_x.

hole mobility was increased from 1.17 × 10^{-4} to 2.95 × 10^{-4}. These results indicate that carriers can be better transported out of devices by using post-annealing treatment, in agreement with the XPS and UPS results.

AFM was employed to study the effect of post-annealing on surface morphology. Fig. 7 shows the AFM images of MoO_x surface of as-deposited and air-annealed devices. All the films show uniform and finely intermixed domains, indicating highly blending of phase in active layer. Large donor–acceptor interfaces can be provided for exciton dissociation. Notably, the post-annealed devices exhibit smoother MoO_x surface. The mean square surface roughness (Rq) was decreased from 0.91 to 0.76 after post-annealing. The smooth surface is favorable to contact with anode and facilitate charge transport, which may be another reason for the improved performance of post-annealed devices.

In addition, to demonstrate the universal applicability of the air annealing method, we also used PDTS–DTffBT, which we reported before,[35,36] as polymer donor to fabricated PSCs and test the effect. The chemical structure of the materials and the J–V curves are showed in Fig. 8(a) and the photovoltaic data are summarized in Table 2. When the PSCs performed with post annealing treatment, the V_{OC} and FF were improved markedly, and the J_{SC} increased slightly, which are the same with the PTB7-Th cases. This suggests that the method may also be applied to PSCs with other polymer donors. Noticing the advanced performance achieved by non-fullerene acceptors, such as the most representative Y6,[37–39] we also used the post-air annealing strategy on Y6-based non-fullerene solar cells. PSC devices using PBDB-T-2F as donor and Y6 as acceptor were fabricated. Fig. 8(b) shows the J–V curves and the data are also listed in Table 2. The results show that the post-air annealing strategy is still effective to improve photovoltaic efficiency in Y6 based non-fullerene solar cells, specially for the FF and V_{OC}. The enhancement percentage is even greater in these high-efficiency devices. This is probably because the efficient PBDB-T-2F:Y6

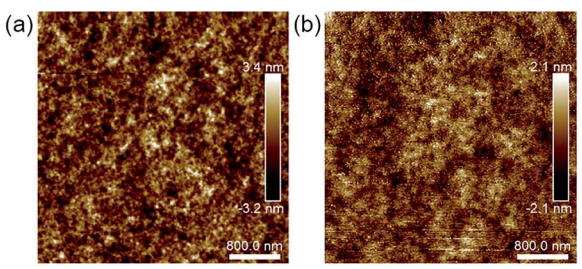

Fig. 7 AFM height images of (a) as-deposited and (b) air-annealed MoO_x surface.

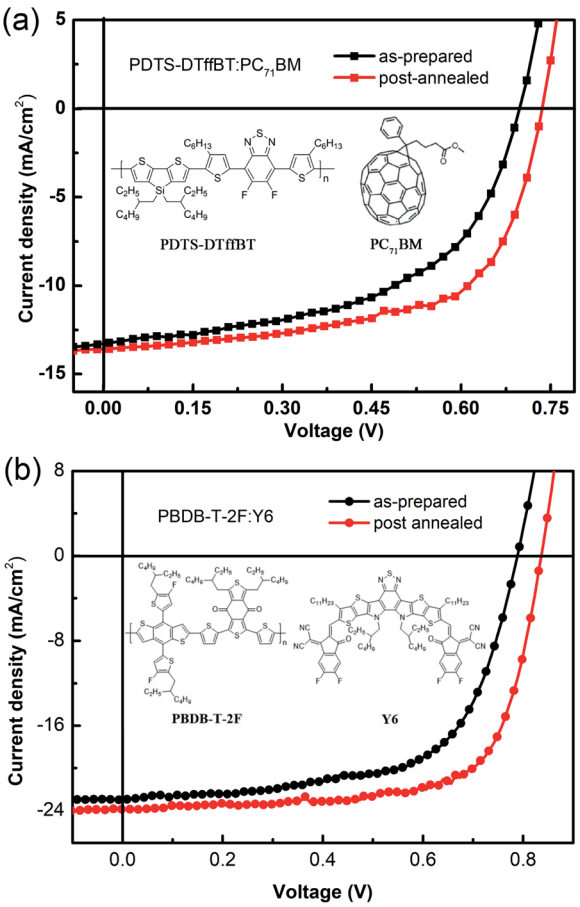

Fig. 8 J–V curves of the as-prepared and post air-annealed PSCs based on (a) PDTS–DTffBT/$PC_{71}BM$ and (b) PBDB-T-2F/Y6 and the chemical structure of the materials.

Table 2 Photovoltaic parameters of the solar cells based on PDTS–DTffBT:$PC_{71}BM$ or PBDB-T-2F:Y6 with different annealed conditions

	V_{OC} (V)	J_{SC} (mA cm^{-2})	FF (%)	PCE (%) Max.	PCE (%) Aver.
PDTS–DTffBT:$PC_{71}BM$ (as-prepared)	0.69 ± 0.01	12.87 ± 0.37	53.17 ± 0.80	4.91	4.74
PDTS–DTffBT:$PC_{71}BM$ (post-annealed)	0.73 ± 0.01	13.55 ± 0.22	62.33 ± 0.42	6.25	6.18
PBDB-T-2F:Y6 (as-prepared)	0.79 ± 0.01	22.61 ± 0.24	62.57 ± 0.61	11.43	11.09
PBDB-T-2F:Y6 (post-annealed)	0.84 ± 0.01	23.72 ± 0.30	69.34 ± 0.52	14.06	13.65

active layers can produce more free carriers and are therefore more sensitive to interfacial energy level mismatch and low efficiency charge extraction.

Experimental

Materials

PTB7-Th were purchased from 1-Material. $PC_{71}BM$ were purchased from Lumtec. PBDB-T-2F and Y6 were purchased from Solarmer Materials Inc. ZnO nanoparticles[40] and PDTS–DTffBT[36] were synthesized according to reported literature, which is described in the ESI.† Other materials were purchased from Aldrich and used without further purification.

Measurements and characterization

XPS and UPS measurements were performed using a VD Scienta R3000 photoelectron spectrometer at ultrahigh vacuum (2×10^{-10} mbar) with a monochromatic Al (Kα) X-ray source (1486.6 eV) and a monochromatic He (Iα) source (21.22 eV), respectively.

TPC measurements were performed using Continuum Minilete TM Nd:YAG laser to shot a 10 ns 532 nm laser pulse with the energy flux of 96.8 μJ cm^{-2}. The laser pulse irradiated through the devices kept at short circuit and the photocurrent was recorded on an oscilloscope (Tektronix MSO 4054) by measuring the voltage drop over a 50 ohm sensing resistor in series with the solar cell.

SCLC measurements were performed using hole-only devices with configuration of ITO/PEDOT:PSS/PTB7-Th:$PC_{71}BM$/MoO_x/Ag. The hole mobilities were calculated by fitting the resulting curves to a space-charge-limited form where SCLC can be described by:

$$J = \frac{9}{8}\varepsilon_0\varepsilon_r\mu_h\frac{(V - V_{bi})^2}{L^3}\exp\left(0.89\beta\sqrt{\frac{V - V_{bi}}{L}}\right)$$

where ε_0 is the permittivity of free space (8.85×10^{-12} F m^{-1}), ε_r is the relative dielectric constant of the conjugated polymers (typically assumed as 3), μ_h is the hole mobility, L is the film thickness of active layer, and β is the field-dependent factor, V_{bi} is the built-in potential due to the WF difference of electrodes caused by contact resistance and series resistance across the electrodes.[41]

AFM images were obtained using Veeco Dimension 3100 instrument working at tapping mode.

MoO_x HTL and PSCs fabrication and characterization

The PSCs were fabricated with inverted structure of ITO/ZnO/active layer/MoO_x/Al. Firstly, patterned ITO substrates (15 Ω Sq^{-1}) were cleaned by ultrasonic using detergent, deionized water, acetone, and isopropyl alcohol sequentially. Then the substrates were fast dried by nitrogen flow followed by UV–ozone treatment for 10 min. After that ZnO nanoparticles dispersion were spin-coated at 3000 rpm for 30 s. The substrates were transferred into muffle furnace and low temperature sintered at 150 °C for 1 hour in air atmosphere. The active layer was prepared in a nitrogen-filled glove box (water and oxygen content less than 0.5 ppm). The PTB7-Th/$PC_{71}BM$ active layer was prepared by dissolving PTB7-Th and $PC_{71}BM$ with weight ratio of 1 : 1.5 in chlorobenzene/1,8-diiodooctane mixed solvent (97 : 3 v/v) with the polymer concentration of 10 mg mL^{-1} and spin coating the blend solution onto the ZnO layer at 3000 rpm for 30 s. The PDTS–DTffBT/$PC_{71}BM$ active layer was prepared by dissolving PDTS–DTffBT and $PC_{71}BM$ with weight ratio of 1 : 2 in chlorobenzene/1,8-diiodooctane mixed solvent (97 : 3 v/v) with the polymer concentration of 10 mg mL^{-1} and spin coating the blend solution at 1200 rpm for 50 s. The PBDB-T-2F/Y6 active layer was prepared by dissolving PBDB-T-2F and Y6 with weight ratio of 1 : 1.2 in chloroform/1-chloronaphthalene mixed solvent (99.5 : 0.5 v/v) with the polymer concentration of 16 mg mL^{-1} and spin coating the blend solution at 3000 rpm for 30 s.[37] The MoO_x HTL (6 nm thick) was prepared using vacuum vapor phase deposition method. The vacuum of the evaporation chamber should be controlled below 1×10^{-5} pa. After the deposition of MoO_x, the substrates with ZnO layer, active layer and MoO_x layer was post-annealed at 90 °C for 10 min in air atmosphere on a hot plate. 90 nm Al cathode was vacuum evaporated to finish the fabrication. For the control devices, the post-air annealing process was skipped, the Al cathode was evaporated immediately after the deposition of MoO_x layer. 10 optimized devices were fabricated and measured for each condition.

Conclusions

We have demonstrated that the oxidation state and WF of MoO_x buffer layer can be raised by post-air annealing strategy, which provide stronger driving force for charge transport. Better photovoltaic performance can be achieved by PSCs based on the post-air annealed MoO_x HTL. For metal oxide semiconductor materials as buffer layer, MoO_x films with higher oxidation state is more in line with the principle of selection. The results provide theoretical and experimental support for improving the performance of optoelectronic devices.

Conflicts of interest

There are no conflicts to declare.

Acknowledgements

This work was supported by National Natural Science Foundation of China (Grant No. 62004081, 11904126), Science and Technology Project of Jilin Provincial Education Department (Grant No. JJKH20180550KJ, JJKH20200250KJ), Scientific and Technological Innovation Development Plan Project of Jilin City (Grant No. 201831777), Scientific Research Project of Jilin Institute of Chemical Technology (Grant No. 2018016, 2021004).

References

1 G. Yu, J. Gao, J. C. Hummelen, F. Wudl and A. J. Heeger, *Science*, 1995, **270**, 1789–1791.
2 J. Brabec, N. S. Saricifici and J. C. Hummelen, *Adv. Funct. Mater.*, 2001, **11**, 15–26.
3 M. Helgesen, R. Søndergaard and F. C. Krebs, *J. Mater. Chem.*, 2010, **20**, 36–60.
4 F. C. Krebs, J. Fyenbo and M. Jørgensen, *J. Mater. Chem.*, 2010, **41**, 8994–9001.
5 Y. Sun, Y. Zhang, Q. Liang, Y. Zhang, H. Chi, Y. Shi and D. Fang, *RSC Adv.*, 2013, **30**, 11925–11934.
6 L. Zhan, S. Li, X. Xia, Y. Li, X. Lu, L. Zuo, M. Shi and H. Chen, *Adv. Mater.*, 2021, **33**, 2007231.
7 T. Zhang, C. An, P. Bi, Q. Lv, J. Qin, L. Hong, Y. Cui, S. Zhang and J. Hou, *Adv. Energy Mater.*, 2021, 2101705.
8 Q. Liu, Y. Jiang, K. Jin, J. Qin, J. Xu, W. Li, J. Xiong, J. Liu, Z. Xiao, K. Sun, S. Yang, X. Zhang and L. Ding, *Sci. Bull.*, 2020, **65**, 272–275.
9 H. J. Son, F. He, B. Carsten and L. Yu, *J. Mater. Chem.*, 2011, **21**, 18934–18945.
10 R. K. Pai, T. N. Ahipa and B. Hemavathi, *RSC Adv.*, 2016, **6**, 23760–23774.
11 R. K. Gupta, R. Garai, M. Hossain, M. A. Afroz, D. Kalita and P. Krishnanlyer, *J. Mater. Chem. C*, 2021, **9**, 8746–8775.
12 V. Malytskyi, J. J. Simon, L. Patrone and J. M. Raimundo, *RSC Adv.*, 2015, **5**, 354–397.
13 P. Ma, C. Wang, S. Wen, L. Wang, L. Shen, W. Guo and S. Ruan, *Sol. Energy Mater. Sol. Cells*, 2016, **155**, 30–37.
14 O. Adebanjo, P. P. Maharjan, P. Adhikary, M. Wang, S. Yang and Q. Qiao, *Energy Environ. Sci.*, 2013, **6**, 3150–3170.
15 Z. Shi, Y. Bai, X. Chen, R. Zeng and Z. Tan, *Sustainable Energy Fuels*, 2019, **3**, 910–934.
16 E. D. Gomez and Y. L. Loo, *J. Mater. Chem.*, 2010, **20**, 6604–6611.
17 G. Li, C. W. Chu, V. Shrotriya, J. Huang and Y. Yang, *Appl. Phys. Lett.*, 2006, **88**, 253503.
18 M. Campoy-Quiles, T. Ferenczi, T. Agostinelli, P. G. Etchegoin, Y. Kim, T. D. Anthopoulos, P. N. Stavrinou, D. D. C. Bradley and J. Nelson, *Nat. Mater.*, 2008, **7**, 158–164.
19 Z. He, C. Zhong, S. Su, M. Xu, H. Wu and Y. Cao, *Nat. Photonics*, 2012, **6**, 591–595.
20 R. Po, C. Carbonera, A. Bernardi and N. Camaioni, *Energy Environ. Sci.*, 2011, **4**, 285–310.
21 Z. Liang, Q. Zhang, L. Jiang and G. Cao, *Energy Environ. Sci.*, 2015, **8**, 3442–3476.
22 Y. Ono, T. Akiyama, S. Banya, D. lzumoto, J. Saito, K. Fujita, H. Sakaguchi, A. Suzuki and T. Oku, *RSC Adv.*, 2014, **4**, 34950–34954.
23 R. Lampande, G. W. Kim, R. Pode and J. H. Kwon, *RSC Adv.*, 2014, **4**, 49855–49860.
24 V. Shrotriya, G. Li, Y. Yao, C. W. Chu and Y. Yang, *Appl. Phys. Lett.*, 2006, **88**, 073508.
25 M. G. Varnamkhasti, H. R. Fallah, M. Mostajaboddavati, R. Ghasemi and A. Hassanzadeh, *Sol. Energy Mater. Sol. Cells*, 2012, **98**, 379–384.
26 J. Meyer, S. Hamwi, M. Kröger, W. Kowalsky, T. Riedl and A. Kahn, *Adv. Mater.*, 2012, **24**, 5408–5427.
27 E. Itoh and S. Nakagoshi, *Jpn. J. Appl. Phys.*, 2014, **53**, 502–503.
28 F. Liu, S. Shao, X. Guo, Y. Zhao and Z. Xie, *Sol. Energy Mater. Sol. Cells*, 2010, **94**, 842–845.
29 J. Meyer, S. Hamwi, M. Kröger, W. Kowalsky, T. Riedl and A. Kahn, *Adv. Mater.*, 2012, **24**, 5408–5427.
30 K. H. Wong, K. Ananthanarayanan, J. Luther and P. Balaya, *J. Phys. Chem. C*, 2012, **116**, 16346–16351.
31 W. Zhao, D. Qian, S. Zhang, S. Li, O. Inganas, F. Gao and J. Hou, *Adv. Mater.*, 2016, **28**, 4734–4739.
32 T. S. Sian and G. B. Reddy, *Sol. Energy Mater. Sol. Cells*, 2004, **82**, 375–386.
33 P. C. Kao, Z. H. Chen, H. E. Yen, T. H. Liu and C. L. Huang, *Jpn. J. Appl. Phys.*, 2018, **57**, 03DA04.
34 J. Liang, F. S. Zu, L. Ding, M. F. Xu, X. B. Shi, Z. K. Wang and L. S. Liao, *Appl. Phys. Express*, 2014, **7**, 111601.
35 P. Ma, S. Wen, C. Wang, W. Guo, L. Shen, W. Dong, J. Lu and S. Ruan, *J. Phys. Chem. C*, 2016, **120**, 19513–19520.
36 S. Wen, C. Wang, P. Ma, Y. Zhao, C. Li and S. Ruan, *J. Mater. Chem. A*, 2015, **3**, 13794–13800.
37 J. Yuan, Y. Zhang, L. Zhou, G. Zhang, H. L. Yip, T. K. Lau, X. Lu, C. Zhu, H. Peng, P. A. Johnson, M. Leclerc, Y. Cao, J. Ulanski, Y. Li and Y. Zou, *Joule*, 2019, **3**, 1140–1151.
38 Y. Lin, B. Adilbekova, Y. Firdaus, E. Yengel, H. Faber, M. Sajjad, X. Zheng, E. Yarali, A. Seitkhan, O. M. Bakr, A. El-Labban, U. Schwingenschlögl, V. Tung, I. McCulloch, F. Laquai and T. D. Anthopoulos, *Adv. Mater.*, 2019, **31**, 1902965.
39 X. Guo, Q. Fan, J. Wu, G. Li, Z. Peng, W. Su, J. Lin, L. Hou, Y. Qin, H. Ade, L. Ye, M. Zhang and Y. Li, *Angew. Chem., Int. Ed.*, 2021, **60**, 2322–2329.
40 C. Wang, C. Li, S. Wen, P. Ma, Y. Liu, R. C. I. Mackenzie, W. Tian and S. Ruan, *J. Mater. Chem. A*, 2017, **5**, 3995–4002.
41 W. Liu, P. Ma, J. Xu, C. Wang, C. Wang, M. Qu and S. Wen, *Phys. Status Solidi A*, 2021, **218**, 2000650.